SCATTERING OF ACOUSTIC AND ELASTIC WAVES USING A HYBRID MULTIPLE MULTIPOLE EXPANSIONS-FINITE ELEMENT TECHNIQUE

Matthias G. Imhof

Earth Resources Laboratory
Department of Earth, Atmospheric, and Planetary Sciences
Massachusetts Institute of Technology
Cambridge, MA 02139

ABSTRACT

In this paper, two different methods to solve scattering problems in acoustic or elastic media are coupled to enhance their usefulness. The multiple multipole (MMP) expansions are used to solve for the scattered fields in homogeneous regions which are possibly unbounded. The finite element (FE) method is used to calculate the scattered fields in heterogeneous but bounded scatterers. As the MMP method requires, the different regions and methods are coupled together in the least squares sense. For some examples, the scattered fields are calculated and compared to the analytical solutions. Finally, the seismograms are calculated for a scattering problem with several scatterers, and complex geometries. Thus, the hybrid MMP-FEM technique is a very general and useful tool to solve complex, two-dimensional scattering problems.

INTRODUCTION

Wave scattering problems have been investigated by different techniques. Analytical solutions to the integral equations do generally not exist except for some very simple geometries. Analytical mode expansion is limited to geometries such as circular cylinders or spheres where the modes decouple (Pao and Mow, 1973). Therefore, numerical schemes seem to be the most direct procedure for arbitrary geometries. Numerical boundary integral techniques (Schuster and Smith, 1985), the T-matrix method (Waterman, 1969, 1976) and MMP expansions (Hafner, 1990; Imhof, 1995a,b) are examples thereof. Unfortunately, they all depend on either Greens functions or other solutions to the wave equation which tend to be hard or impossible to find for heterogeneous or anisotropic media. Thus, these methods are normally limited to scattering between ho-

mogeneous scatterers embedded in a homogeneous background. As an advantage, these methods do not encounter problems with unbounded domains. No artificial radiating boundary conditions have to be enforced. In fact, the scattered fields can be evaluated anywhere.

In cases where the medium is heterogeneous, finite element (FE) (Zienkiewicz, 1977; Schwarz, 1988; Murphy and Chin-Bing, 1989, 1991; Marfurt, 1984) or finite differences (FD) (Marfurt, 1984; Kelly *et al.*, 1976; Virieux, 1986) techniques are routinely used to calculate the scattered wavefields. Opposed to the boundary methods mentioned priorly, FE and FD encounter serious problems with unbounded domains. The domain has to be truncated and radiating boundary conditions have to be enforced. Even if the domains are bounded, they are limited due to computer memory and runtime considerations. For many problems the distance, between inhomogeneities, source and receivers are rather large and thus result in prohibitive computation times and memory requirements.

Many scattering problems exist which fall in between these two classes. These problems involve heterogeneous regions which are bounded and embedded in a homogeneous background. Therefore, there is an obvious interest in combining methods for unbounded, homogeneous domains with methods which can handle heterogeneous regions of limited extent (Su, 1983; Dubus, 1994). In the present paper, such a combination is made between the MMP expansions and the FE method (FEM).

We will apply the hybrid technique to both acoustic and elastic in-plane scattering problems where one or multiple heterogeneities are embedded in a homogeneous medium. Both source and receiver are in the homogeneous region. All the ideas presented will also hold if the source and receiver are located in the heterogeneity. We could then use the combined MMP-FEM technique to construct the radiating boundary condition. In this work, we will not investigate this usage of the technique. Also, we will neglect the case of anti-plane wave motion (SH) because it can easily be derived from the acoustic case.

This paper is structured as follows: First, we will review both MMP expansions and the finite element method for the acoustic case. Next, we combine the methods for the acoustic case. Then, we review MMP and FEM in the elastic case and present the combination thereof. Finally, we discuss some details of the implementation on a computer, present solutions to some scattering problems and compare them to analytical solutions where available.

ACOUSTIC THEORY

We would like to model how an incident wavefield $p^{inc}(\vec{x}, \omega)$ of angular frequency ω scatters from an object. The situation is depicted in Figure 1. The scatterer Ω^I is heterogeneous and embedded in a homogeneous background Ω^O. For the sake of clarity, we will suppress the time factor $e^{-i\omega t}$ in all following expressions. Where necessary, the superscripts ^{O}, ^{B} and ^{I} will denote quantities which belong to the homogeneous

outside, lie on the boundary between the domains or are inside the heterogeneous region, respectively. Quantities marked with a tilde are either transformed quantities (e.g., LU decomposed) or local quantities for one particular little element $\tilde{\Omega}$ where the context allows to infer the correct meaning.

Homogeneous Regions: Multiple Multipole Expansions

In a homogeneous region Ω^O, expansions for the pressure fields are made with exact solutions to the homogeneous wave equation

$$(1) \qquad P^O(\mathbf{x}) = \sum_{j=1}^{J^O} p_j^O P_j^O(\mathbf{x}) \qquad \text{where} \qquad \forall P_j^O : (\nabla^2 + k_O^2)P_j^O = 0$$

where $k_O = \omega/\alpha_O$ is the wave number and α_O the wave velocity in the homogeneous region. The factors p_j^O are complex valued weighting coefficients for the different expansion functions P_j^O. As the name of the method implies, several multipole solutions centered at different positions are often used as expansion functions. The reason to use multiple multipole expansions is their local behavior and thus their ability to model wavefields scattered from complex geometries (Imhof, 1995a).

$$(2) \qquad P^O(\mathbf{x}) = \sum_{m=1}^{M} \sum_{n=-N}^{N} p_{mn}^O e^{in\varphi} H_{|n|}^{(1)} (k_O |\mathbf{x} - \mathbf{x}_m|)$$

The function $H_{|n|}^{(1)}$ is the Hankel function of the first kind and order n radiating outward. Each summation over the index n builds up one multipole. To enhance the convergence, M different expansion centers located at $\mathbf{x}_m$ are used. Since the Hankel functions have a singularity at their origin, the centers of expansions $\mathbf{x}_m$ may not be located in the homogeneous region Ω^O. For each expansion center, all orders between $-N \leq n \leq +N$ are used as basis functions.

However, additional expansion functions, such as plane waves or other special modes, can be included. As a result, MMP expansions have, in general, a smaller number of unknowns than comparable methods. Equations for the weighting coefficients p_j^O are obtained by enforcing boundary conditions for the pressure and the normal displacement on discrete matching points $\mathbf{m}_i$ on the boundaries between domains. The boundary conditions between two domains Ω^O and Ω^X are

$$(3) \qquad \sum_{1}^{J^O} p_j^O P_j^O(\mathbf{m}_i) + P^{inc}(\mathbf{m}_i) \;=\; P^X(\mathbf{m}_i)$$

$$(4) \qquad \frac{-1}{k_O^2 \lambda^O} \hat{n}_i \cdot \sum_{1}^{J^O} p_j^O \nabla P_j^O(\mathbf{m}_i) + \frac{-1}{k_O^2 \lambda^O} \hat{n}_i \cdot \nabla P^{inc}(\mathbf{m}_i) \;=\; \frac{-1}{k_X^2 \lambda^X} \hat{n}_i \cdot \nabla P^X(\mathbf{m}_i)$$

where it is assumed that the only source is the incident field P^{inc} in the homogeneous domain Ω^O. Thus, we can build the following linear equation system

$$(5) \qquad \begin{pmatrix} \mathbf{P}^O \\ \mathbf{U}^O \end{pmatrix} \cdot \mathbf{p}^O = \begin{pmatrix} \mathbf{P}^X - \mathbf{P}^{inc} \\ \mathbf{U}^X - \mathbf{U}^{inc} \end{pmatrix}$$

where the submatrices P_{ij}^O and U_{ij}^O contain P_j^O and $\frac{-1}{k_O^2 \lambda^O} \hat{n}_i \cdot \nabla P_j^O$ evaluated at the matching points m_i. In general, expansions of the form (1) are not orthogonal. Thus, more matching points than needed are used and the resulting overdetermined linear system (5) is solved in the *least square sense* minimizing the overall error in the boundary conditions. Due to their definition, the matrices $\mathbf{P}^O$ and $\mathbf{U}^O$ are rectangular and dense matrices.

Heterogeneous Regions: Finite Elements

Neglecting source terms, waves propagating in an heterogeneous region Ω^I are governed by the general Helmholtz equation.

$$(6) \qquad \nabla \cdot \left\{ \rho^{-1} \nabla P \right\} + \rho^{-1} k^2 \, P = 0)$$

where $\rho = \rho(\mathbf{x})$ and $k = k(\mathbf{x})$ denote density and wave number, respectively.

To solve this equation, we partition heterogeneous domain Ω^I into small and nonoverlapping elements $\tilde{\Omega}$ (Zienkiewicz, 1977; Schwarz, 1988; Murphy and Chin-Bing, 1989). Commonly, one chooses triangular or quadrangular elements. In each element, the pressure field $\tilde{P}$ is approximated by an interpolation function. For a quadrangular element, the most simple interpolation function to use is the bilinear one:

$$(7) \qquad \tilde{P}(\mathbf{x}) = a_0 + a_1 x + a_2 z + a_3 x z$$

Instead of directly using the coefficients a_j, the polynomial (7) is transformed into the sum of simple shape functions $\tilde{N}_j(\mathbf{x})$ having local support only. For example, in a rectangular element of unit size, $\tilde{N}_3(\mathbf{x}) = xz$. This shape function is visualized in Figure 2. The other ones are obtained by rotations of $-180°$, $-90°$ and $90°$.

$$(8) \qquad \tilde{P}(\mathbf{x}) = \sum_{j=1}^{4} \tilde{p}_j \tilde{N}_j(\mathbf{x})$$

In fact, the complex valued weighting coefficients $\tilde{p}_j$ are the pressure values at the element's corners $\tilde{x}_i$. They are also known as node points. The coefficients $\tilde{p}_j$ are called node variables. Also, the interpolation functions have to satisfy the following conditions:

$$(9) \qquad \tilde{N}_j(\tilde{x}_i) = \delta_{ij}$$

$$(10) \qquad \sum_{j=1}^{4} \tilde{N}_j(\mathbf{x}) = 1 \quad \text{for} \quad \mathbf{x} \in \tilde{\Omega}$$

Thus, the pressure in the Helmholtz equation (6) is replaced by the interpolation (8). Applying Galerkin's method, we multiply the resulting expression by the test function $\tilde{N}_i(\mathbf{x})$ and integrate over the element $\tilde{\Omega}$.

$$(11) \quad \sum_{j=1}^{4} \left\{ \iint_{\tilde{\Omega}} \rho^{-1} \, \nabla \tilde{N}_i \cdot \nabla \tilde{N}_j \, dA - \iint_{\tilde{\Omega}} \rho^{-1} k^2 \, \tilde{N}_i \tilde{N}_j \, dA \right\} \tilde{p}_j - \int_{\tilde{\Gamma}} \rho^{-1} \tilde{N}_i \frac{\partial P}{\partial n} \, dl = 0$$

where the divergence theorem is used to transform the first integral. The integrals are over the surface $\tilde{\Omega}$ or around the boundary $\tilde{\Gamma}$ of the element $\tilde{\Omega}$, respectively. Evaluating (11) for all four $\tilde{N}_i(\mathbf{x})$ will yield a set of four equations for the four unknown node variables $\tilde{p}_j$.

These three integrals define the local stiffness matrix $\tilde{\mathbf{S}}$, the local mass matrix $\tilde{\mathbf{M}}$ and the local force vector $\tilde{\mathbf{f}}$.

$$(12) \qquad \tilde{S}_{ij} \quad = \quad \iint_{\tilde{\Omega}} \rho^{-1} \, \nabla \tilde{N}_i \cdot \nabla \tilde{N}_j \, dA$$

$$(13) \qquad \tilde{M}_{ij} \quad = \quad \iint_{\tilde{\Omega}} \rho^{-1} k^2 \, \tilde{N}_i \tilde{N}_j \, dA$$

$$(14) \qquad \tilde{f}_i \quad = \quad \int_{\tilde{\Gamma}} \rho^{-1} \tilde{N}_i \frac{\partial P}{\partial n} \, dl$$

For elements that are in the interior, the boundary integral (14) is not zero, but its contributions will exactly cancel with like terms coming from neighboring elements. One only need to recall that the term $\rho^{-1} \frac{\partial P}{\partial n}$ is proportional to the normal displacement. But both the normal displacement and the pressure are continuous across boundaries. Therefore, only on the domain boundary the line integral has to be taken into account since it is not cancelled by another term.

If the element $\tilde{\Omega}$ is adjacent to a rigid domain, the boundary integral (14) will vanish, since $\tilde{N}_i = 0$. If the element is adjacent to a void domain, the integral (14) also vanishes because $\frac{\partial P}{\partial n} = 0$. In all other cases, the boundary integral (14) has to be included. Assuming that $\frac{\partial P}{\partial n}$ can be approximated by a function similar to $\tilde{N}_i$ along the boundary, we can replace (14) by

$$(15) \qquad \tilde{f}_i = \sum_{j=1}^{4} \tilde{F}_{ij} \frac{\partial P(\mathbf{x}_j)}{\partial n} \qquad \tilde{F}_{ij} = \int_{\tilde{\Gamma}} \rho^{-1} \tilde{N}_i \tilde{N}_j \, dl.$$

If the density ρ and the wavenumber k are treated as constants within each element, $\tilde{\mathbf{S}}$, $\tilde{\mathbf{M}}$ and $\tilde{\mathbf{F}}$ can be evaluated exactly. Once the contribution of the various elements is determined, the global system of equations is formed by mapping the local node numbers onto the global node numbers, giving rise to the global pressure vector $\mathbf{p}$, and combining all of the subsystems $\tilde{\mathbf{S}}$, $\tilde{\mathbf{M}}$ and $\tilde{\mathbf{f}}$ into their global counterparts $\mathbf{S}$, $\mathbf{M}$ and $\mathbf{f}$ (Schwarz, 1988). Both matrices $\mathbf{S}$ and $\mathbf{M}$ are sparse, banded and symmetric. Each row of the global matrix system can then be reduced to

$$(16) \qquad \sum_{j=1}^{J} \left\{ (S_{ij} - M_{ij}) \cdot p_j - F_{ij} \cdot \frac{\partial P(\mathbf{x}_j)}{\partial n} \right\} = 0$$

where J is the total number of node variables or in simpler matrix form

$$(17) \qquad\qquad \mathbf{K} \cdot \mathbf{p} - \mathbf{f} = 0$$

where $\mathbf{K} = \mathbf{S} - \mathbf{M}$ and the vector $\mathbf{p}$ contains all the unknown, global nodal values p_j.

Coupling the Regions

The vector $\mathbf{p}$ obtained from the finite elements containing the node variables can be split into two subvectors $\mathbf{p}^I$ and $\mathbf{p}^B$. The node variables from inside the domain Ω^I are collected in the vector $\mathbf{p}^I$. The subvector $\mathbf{p}^B$ accommodates the node variables whose nodal points $\mathbf{x}_i$ lie on the boundary $\partial\Omega^B$. Since the boundary $\partial\Omega^B$ belongs to both domains, the respective wavefields P^O and P^B have to match along the boundary.

Thus we replace the node variables p_i^B by

$$(18) \qquad\qquad p_i^B = \sum_{k=1}^{J^O} p_k^O P_k(\mathbf{x}_i) + P^{inc}(\mathbf{x}_i)$$

Furthermore, we can also find $\frac{\partial P(\mathbf{x}_i)}{\partial n}$ by evaluating

$$(19) \qquad\qquad \frac{\partial P(\mathbf{x}_i)}{\partial n} = \sum_{k=1}^{J^O} p_k^O \hat{n}_i \nabla P_k(\mathbf{x}_i) + \hat{n}_i \nabla P^{inc}(\mathbf{x}_i)$$

Combining (16), (18) and (19) yields the hybrid matrix system

$$(20) \quad \sum_{j=1}^{J^I} \left\{ K_{ij} \cdot p_j \right\} + \sum_{j=J^B}^{J} \left\{ K_{ij} \cdot \sum_{k=1}^{J^O} p_k^O P_k(\mathbf{x}_j) - F_{ij} \cdot \sum_{k=1}^{J^O} p_k^O \hat{n}_j \nabla P_k(\mathbf{x}_j) \right\} =$$

$$\sum_{j=J^B}^{J} \left\{ F_{ij} \cdot \hat{n}_j \nabla P^{inc}(\mathbf{x}_j) - K_{ij} \cdot P^{inc}(\mathbf{x}_j) \right\}$$

where J^I is the total number of node variables inside the heterogeneous region Ω^I. J^B is the node number of the first nodal point lying on the boundary $\partial\Omega^B$. The value of J^B is $J^I + 1$. As before, J is the total number of node points. Finally, J^O is the total number of functions used for the MMP expansion of the outside field. The complete system can be written in a more compact form as

$$(21) \qquad\qquad \begin{pmatrix} \mathbf{A}^{II} & \mathbf{A}^{IO} \\ \mathbf{A}^{OI} & \mathbf{A}^{OO} \end{pmatrix} \cdot \begin{pmatrix} \mathbf{p}^I \\ \mathbf{p}^O \end{pmatrix} = \begin{pmatrix} \mathbf{f}^I \\ \mathbf{f}^O \end{pmatrix}$$

where $\mathbf{A}^{II}$ is a sparse, diagonally dominant and symmetric matrix. Both $\mathbf{A}^{IO}$ and $\mathbf{A}^{OI}$ are sparse and rectangular, while $\mathbf{A}^{OO}$ is rectangular, but dense matrix. The force vector $\mathbf{f}^I$ is sparse, while $\mathbf{f}^O$ is completely filled.

The matrix $\mathbf{A}^{II}$ and the solution vector $\mathbf{p}^I$ stem from the interior problem which is solved by FE. It contains as many equations as unknowns and can be solved exactly. The matrices $\mathbf{A}^{IO}$ and $\mathbf{A}^{OI}$ couple the interior problem to the exterior problem and vice versa. The matrix $\mathbf{A}^{OO}$ and the solution vector $\mathbf{p}^O$ stem from the exterior problem which is solved by MMP expansions. It has to be solved in the least squares sense because there are more equations needed than unknowns given. Therefore, the complete matrix system (21) can not be solved exactly. Contrarily, it does neither mathematically nor physically make sense to solve the complete system (21) in the least squares sense. Prior experience with MMP methods shows that at least twice as many equations as unknowns are needed to obtain a reasonable solution (Imhof, 1995b). Unfortunately, there are in general more unknowns in the interior than in the exterior. Thus, it is nearly impossible to obtain more than twice as many equations as unknowns. Furthermore, the solution in the interior is already an approximation to the wave equation. Solving the complete system in the least squares sense distributes the errors evenly over all unknowns which corrupts the solution in the interior further.

Therefore, the system (21) is solved in two steps: first, the interior node variables $\mathbf{p}^I$ are eliminated by a partial Gaussian elimination. Because the corresponding submatrix $\mathbf{A}^{II}$ is derived with the finite elements method and thus diagonally dominant, the Gaussian elimination can be performed without additional pivoting.

$$(22) \qquad \begin{pmatrix} \tilde{\mathbf{A}}^{II} & \tilde{\mathbf{A}}^{IO} \\ 0 & \tilde{\mathbf{A}}^{OO} \end{pmatrix} \cdot \begin{pmatrix} \tilde{\mathbf{p}}^I \\ \tilde{\mathbf{p}}^O \end{pmatrix} = \begin{pmatrix} \tilde{\mathbf{f}}^I \\ \tilde{\mathbf{f}}^O \end{pmatrix}$$

The submatrix $\tilde{\mathbf{A}}^{II}$ is now an upper triangular matrix. The remaining system can then be solved in the least squares sense using the normal equations

$$(23) \qquad \left(\tilde{\mathbf{A}}^{OO}\right)^H \cdot \tilde{\mathbf{A}}^{OO} \cdot \mathbf{p}^O = \left(\tilde{\mathbf{A}}^{OO}\right)^H \cdot \tilde{\mathbf{f}}^O$$

where the superscript ^{H} denotes the complex conjugate transpose. If desired, the values of the node variables $\mathbf{p}^I$ are found by back-substitution.

$$(24) \qquad \tilde{\mathbf{A}}^{II} \cdot \mathbf{p}^I = \tilde{\mathbf{f}}^I - \tilde{\mathbf{A}}^{IO} \cdot \mathbf{p}^O$$

Practically, the system (21) is solved by a combined, row-wise LU-QR algorithm. From each new row, the interior node variables are Gaussian eliminated. Then, Givens row updating (schwarz, 1989) is performed on the remaining row. The scheme is equal to normal Givens updating with the first J^I Givens rotations replaced by Gaussian eliminations instead. Thus, the first J^I rows are only LU decomposed. All other rows are additionally Givens rotated.

Remark: An Alternative Solver Scheme

Alternatively, the system (21) can be solved by the iterative scheme:

$$(25a) \qquad \mathbf{A}^{II} \cdot \mathbf{p}_n^I = \mathbf{f}^I - \mathbf{A}^{IO} \cdot \mathbf{p}_{n-1}^O$$

$$(25b) \qquad \mathbf{A}^{OO} \cdot \mathbf{p}_n^O = \mathbf{f}^O - \mathbf{A}^{OI} \cdot \mathbf{p}_{n-1}^I$$

Optimally, each of (25a) and (25b) is also solved by an iterative scheme such as the conjugate gradient method (Hestenes and Stiefel, 1952). The first part (25a) is square, symmetric and sparse. The second part (25b) is rectangular and dense, but relatively small compared to (25a). The scheme (25) offers an alternative to (21), but this has not yet been tried.

ELASTIC THEORY

Homogeneous Regions: Multiple Multipole Expansions

In a homogeneous region Ω^O, expansions for the displacement fields $\mathbf{w}(\mathbf{x}) = (u(\mathbf{x}), v(\mathbf{x}))$ are made with exact solutions to the homogeneous wave equation (Imhof, 1995b).

$$(26) \qquad \mathbf{w}(\mathbf{x}) = \sum_{j=1}^{J^O} \left\{ \phi_j \mathbf{w}_j^{\Phi}(\mathbf{x}) + \psi_j \mathbf{w}_j^{\Psi}(\mathbf{x}) \right\}$$

where

$$(27a) \qquad \mathbf{w}_j^{\Phi}(\mathbf{x}) \;=\; \nabla \Phi_j(\mathbf{x})$$

$$(27b) \qquad \mathbf{w}_j^{\Psi}(\mathbf{x}) \;=\; \nabla \times (\hat{y} \Psi_j(\mathbf{x}))$$

and each expansion function Φ_j or Ψ_j satisfies a Helmholtz equation

$$(28a) \qquad (\nabla^2 + k_O^2)\Phi_j = 0$$

$$(28b) \qquad (\nabla^2 + l_O^2)\Psi_j = 0$$

where k_O and l_O are the the wave numbers of the P-, respective S-wave in the homogeneous region. The factors ϕ_j and ϕ_j are complex valued weighting coefficients for the different expansion functions Φ_j and Ψ_j. Similar to the acoustic MMP expansions (2), we choose multipole expansions for Φ_j and Ψ_j.

$$(29a) \qquad \Phi(\mathbf{x}) \;=\; \sum_{m=1}^{M} \sum_{n=-N}^{N} \phi_{mn} e^{in\varphi} H_{|n|}^{(1)} \left(k_O \, |\mathbf{x} - \mathbf{x}_m| \right)$$

$$(29b) \qquad \Psi(\mathbf{x}) \;=\; \sum_{m=1}^{M} \sum_{n=-N}^{N} \psi_{mn} e^{in\varphi} H_{|n|}^{(1)} \left(l_O \, |\mathbf{x} - \mathbf{x}_m| \right)$$

Equations for the weighting coefficients ϕ_j and ψ_j are obtained by enforcing boundary conditions along discrete matching points $\mathbf{m}_i$ on the boundaries between domains. The boundary conditions between two domains Ω^O and Ω^X are continuity of displace-

ment and stresses in normal and tangential directions:

(30)
$$\sum_{j=1}^{J^O} \left\{ \phi_j u_j^\Phi(\mathbf{m}_i) + \psi_j u_j^\Psi(\mathbf{m}_i) \right\} + u^{inc}(\mathbf{m}_i) = u^X(\mathbf{m}_i)$$

(31)
$$\sum_{j=1}^{J^O} \left\{ \phi_j v_j^\Phi(\mathbf{m}_i) + \psi_j v_j^\Psi(\mathbf{m}_i) \right\} + v^{inc}(\mathbf{m}_i) = v^X(\mathbf{m}_i)$$

(32)
$$\sum_{j=1}^{J^O} \hat{n}_i \left\{ \phi_j \sigma_j^\Phi(\mathbf{m}_i) + \psi_j \sigma_j^\Psi(\mathbf{m}_i) \right\} \hat{n}_i + \hat{n}_i \, \sigma^{inc}(\mathbf{m}_i) \, \hat{n}_i = \hat{n}_i \, \sigma^X(\mathbf{m}_i) \, \hat{n}_i$$

(33)
$$\sum_{j=1}^{J^O} \hat{t}_i \left\{ \phi_j \sigma_j^\Phi(\mathbf{m}_i) + \psi_j \sigma_j^\Psi(\mathbf{m}_i) \right\} \hat{n}_i + \hat{t}_i \, \sigma^{inc}(\mathbf{m}_i) \, \hat{n}_i = \hat{t}_i \, \sigma^X(\mathbf{m}_i) \, \hat{n}_i$$

where $\sigma_j^\Phi(\mathbf{m}_i)$, $\sigma_j^\Psi(\mathbf{m}_i)$, $\sigma^{inc}(\mathbf{m}_i)$ and $\sigma^X(\mathbf{m}_i)$ denote the stresses evaluated at $\mathbf{m}_i$ due to the displacements $\mathbf{w}_j^\Phi(\mathbf{m}_i)$, $\mathbf{w}_j^\Psi(\mathbf{m}_i)$, $\mathbf{w}_j^{inc}(\mathbf{m}_i)$ and $\mathbf{w}_j^X(\mathbf{m}_i)$, respectively. Accordingly, we can build a linear equation system

(34)
$$\begin{pmatrix} \mathbf{U}^\Phi & \mathbf{U}^\Psi \\ \mathbf{V}^\Phi & \mathbf{V}^\Psi \\ \mathbf{\Sigma}_n^\Phi & \mathbf{\Sigma}_n^\Psi \\ \mathbf{\Sigma}_t^\Phi & \mathbf{\Sigma}_t^\Psi \end{pmatrix} \cdot \begin{pmatrix} \phi \\ \psi \end{pmatrix} = \begin{pmatrix} \mathbf{U}^X - \mathbf{U}^{inc} \\ \mathbf{V}^X - \mathbf{V}^{inc} \\ \mathbf{\Sigma}_n^X - \mathbf{\Sigma}_n^{inc} \\ \mathbf{\Sigma}_t^X - \mathbf{\Sigma}_t^{inc} \end{pmatrix}$$

where the submatrices contain equations (30–33) evaluated at all matching points $\mathbf{m}_i$.

Heterogeneous Regions: Finite Elements

Again neglecting source terms, the equations of motion for elastic medium for the displacement components u and v are

(35a)
$$\omega^2 \rho u + (c_{11} u_{,x} + c_{12} v_{,z})_{,x} + c_{33} (u_{,z} + v_{,x})_{,z} = 0$$

(35b)
$$\omega^2 \rho v + c_{33} (u_{,z} + v_{,x})_{,x} + (c_{12} u_{,x} + c_{22} v_{,z})_{,z} = 0$$

where the density ρ and the elastic constants $c_{11} = c_{22} = \lambda + 2\mu$, $c_{12} = \lambda$ and $c_{33} = \mu$ are all spatially varying. The subscripts $_{,x}$ and $_{,z}$ denote partial derivatives with respect to x or z, respectively.

As in the acoustic case (8), the displacements inside the elements $\tilde{\Omega}$ are approximated by interpolation functions (Zienkiewicz, 1977; Schwarz, 1988; Murphy and Chin-Bing, 1991):

(36a)
$$\tilde{u} = \sum_{j=1}^{4} \tilde{u}_j \tilde{N}_j(\mathbf{x})$$

(36b)
$$\tilde{v} = \sum_{j=1}^{4} \tilde{v}_j \tilde{N}_j(\mathbf{x})$$

The complex valued weighting coefficients $\tilde{u}_j$ and $\tilde{u}_j$ are the components of the displacements at the element's corners $\tilde{x}_i$. The shape functions $\tilde{N}_j(\mathbf{x})$ are the same as in the acoustic case, e.g. $\tilde{N}_3(\mathbf{x}) = xz$ (Figure 2).

In the equation of motion (35), we replace the displacements u and v by the interpolations (36). Applying Galerkin's method for each element $\tilde{\Omega}$, we multiply the resulting expression by the test function $\tilde{N}_i(\mathbf{x})$ and integrate over the element $\tilde{\Omega}$.

$$(37a) \quad \sum_{j=1}^{4} \left\{ \iint_{\tilde{\Omega}} \left(c_{11} \tilde{N}_{i,x} \tilde{N}_{j,x} + c_{33} \tilde{N}_{i,z} \tilde{N}_{j,z} \right) dA - \iint_{\tilde{\Omega}} \rho \omega^2 \, \tilde{N}_i \tilde{N}_j \, dA \right\} \tilde{u}_j +$$

$$\sum_{j=1}^{4} \left\{ \iint_{\tilde{\Omega}} \left(c_{12} \tilde{N}_{i,x} \tilde{N}_{j,z} + c_{33} \tilde{N}_{i,z} \tilde{N}_{j,x} \right) dA \right\} \tilde{v}_j - \int_{\tilde{\Gamma}} \tilde{N}_i \hat{x} \sigma \hat{n} \, dl = 0$$

$$(37b) \quad \sum_{j=1}^{4} \left\{ \iint_{\tilde{\Omega}} \left(c_{12} \tilde{N}_{i,z} \tilde{N}_{j,x} + c_{33} \tilde{N}_{i,x} \tilde{N}_{j,z} \right) dA \right\} \tilde{u}_j -$$

$$\sum_{j=1}^{4} \left\{ \iint_{\tilde{\Omega}} \left(c_{33} \tilde{N}_{i,x} \tilde{N}_{j,x} + c_{22} \tilde{N}_{i,z} \tilde{N}_{j,z} \right) dA - \iint_{\tilde{\Omega}} \rho \omega^2 \, \tilde{N}_i \tilde{N}_j \, dA \right\} \tilde{v}_j - \int_{\tilde{\Gamma}} \tilde{N}_i \hat{z} \sigma \hat{n} \, dl = 0$$

where we used the divergence theorem to transform some of the volume integrals into line integrals. The quantity σ denotes the stress tensor along the boundary. Thus, evaluating (37) for all $\tilde{N}_i(\mathbf{x})$ will yield a set of equations for the unknown node variables $\tilde{u}_j$ and $\tilde{v}_j$. Again, equation (37) defines the stiffness matrices $\tilde{\mathbf{S}}^{ij}$, mass matrices $\tilde{\mathbf{M}}^{ii}$ and the force vectors $\tilde{\mathbf{f}}^i$:

$$(38) \qquad \tilde{M}_{ij}^{11} = \tilde{M}_{ij}^{22} = \iint_{\tilde{\Omega}} \rho \omega^2 \, \tilde{N}_i \tilde{N}_j \, dA$$

$$(39) \qquad \tilde{S}_{ij}^{11} = \iint_{\tilde{\Omega}} \left(c_{11} \tilde{N}_{i,x} \tilde{N}_{j,x} + c_{33} \tilde{N}_{i,z} \tilde{N}_{j,z} \right) dA$$

$$(40) \qquad \tilde{S}_{ij}^{22} = \iint_{\tilde{\Omega}} \left(c_{33} \tilde{N}_{i,x} \tilde{N}_{j,x} + c_{22} \tilde{N}_{i,z} \tilde{N}_{j,z} \right) dA$$

$$(41) \qquad \tilde{S}_{ij}^{12} = \tilde{S}_{ji}^{21} = \iint_{\tilde{\Omega}} \left(c_{12} \tilde{N}_{i,x} \tilde{N}_{j,z} + c_{33} \tilde{N}_{i,z} \tilde{N}_{j,x} \right) dA$$

$$(42) \qquad \tilde{f}_i^1 = \int_{\tilde{\Gamma}} \tilde{N}_i \hat{x} \sigma \hat{n} \, dl$$

$$(43) \qquad \tilde{f}_i^2 = \int_{\tilde{\Gamma}} \tilde{N}_i \hat{z} \sigma \hat{n} \, dl$$

If the density ρ and the elastic constants c_{11}, c_{22}, c_{12} and c_{33} are treated as constants within each element $\tilde{\Omega}$, all integral (38-41) can be evaluated exactly. For elements which are in the interior, the boundary integrals (42,43) are not zero, but its contributions will exactly cancel with like terms coming from neighboring elements because displacements and stresses are continuous across boundaries. Therefore, the line integrals have to be

taken into account only on the domain boundary. Assuming that $\hat{x}\sigma\hat{n}$ and $\hat{z}\sigma\hat{n}$ can be approximated by functions similar to $\tilde{N}_i$ along the boundary, we can replace (42,42) by

$$(44) \qquad \tilde{f}_i^1 = \sum_{j=1}^{4} \tilde{F}_{ij}\hat{x}\sigma(\mathbf{x}_j)\hat{n}$$

$$(45) \qquad \tilde{f}_i^2 = \sum_{j=1}^{4} \tilde{F}_{ij}\hat{z}\sigma(\mathbf{x}_j)\hat{n}$$

$$(46) \qquad \tilde{F}_{ij} = \int_{\tilde{\Gamma}} \tilde{N}_i\tilde{N}_j \, dl$$

which can also be evaluated analytically. Mapping all the local contributions of $\tilde{S}^{ij}$, $\tilde{M}^{ii}$ and $\tilde{f}^i$ into global node numbers yields the global matrices S^{ij}, M^{ii}, f^i and the global nodal vectors $\mathbf{u}$ and $\mathbf{v}$. Writing $K^{ij} = S^{ij} - \delta_{ij}M^{ii}$, the global matrix system reduces to the simpler system

$$(47a) \qquad K^{11}\mathbf{u} + K^{12}\mathbf{v} - f^1 = 0$$
$$(47b) \qquad K^{21}\mathbf{u} + K^{22}\mathbf{v} - f^2 = 0.$$

Coupling the Regions

Each vector $\mathbf{u}$ and $\mathbf{v}$ obtained from the finite elements is split into two subvectors $\mathbf{u}^I$, $\mathbf{u}^B$ and $\mathbf{v}^I$, $\mathbf{v}^B$, respectively. The node variables u_i and v_i from inside the domain Ω^I are collected in the vectors $\mathbf{u}^I$ and $\mathbf{v}^I$, respectively. The subvectors $\mathbf{u}^B$ and $\mathbf{u}^B$ accommodate the node variables whose nodal points $\mathbf{x}_i$ lie on the boundary $\partial\Omega^B$. Since the boundary $\partial\Omega^B$ belongs to both domains, the respective wavefields $\mathbf{w}^O$ and $\mathbf{w}^B$ have to match along the boundary and we can replace the node variables u_j^B and v_j^B by

$$(48a) \qquad u_j^B = \cdot \sum_{k=1}^{J^O} \left\{ \phi_k u_k^{\Phi}(\mathbf{x}_j) + \psi_k u_k^{\Psi}(\mathbf{x}_j) \right\} + u^{inc}(\mathbf{x}_j)$$

$$(48b) \qquad v_j^B = \hat{z} \cdot \sum_{k=1}^{J^O} \left\{ \phi_k v_k^{\Phi}(\mathbf{x}_j) + \psi_k v_k^{\Psi}(\mathbf{x}_j) \right\} + v^{inc}(\mathbf{x}_j).$$

Furthermore, we find $\sigma(\mathbf{x}_j)$ by evaluating

$$(49) \qquad \sigma(\mathbf{x}_j) = \sum_{k=1}^{J^O} \left\{ \phi_k \sigma_k^{\Phi}(\mathbf{x}_j) + \psi_k \sigma_k^{\Psi}(\mathbf{x}_j) \right\} + \sigma^{inc}(\mathbf{x}_j)$$

Combining (47), (48) and (49) yields the coupled MMP-FEM system. For the sake of clarity, we explicitly expand (47a):

$$(50) \quad \sum_{j=1}^{J^I} \left\{ K_{ij}^{11} \cdot u_j + K_{ij}^{12} \cdot v_j \right\} +$$

$$\sum_{j=J^B}^{J} \left\{ K_{ij}^{11} \cdot \sum_{k=1}^{J^O} \left\{ \phi_k u_k^\Phi(\mathbf{x}_j) + \psi_k u_k^\Psi(\mathbf{x}_j) \right\} + K_{ij}^{12} \cdot \sum_{k=1}^{J^O} \left\{ \phi_k v_k^\Phi(\mathbf{x}_j) + \psi_k v_k^\Psi(\mathbf{x}_j) \right\} \right\} -$$

$$\sum_{j=J^B}^{J} \left\{ F_{ij} \cdot \sum_{k=1}^{J^O} \hat{x} \left\{ \phi_k \sigma_k^\Phi(\mathbf{x}_j) + \psi_k \sigma_k^\Psi(\mathbf{x}_j) \right\} \hat{n} \right\} =$$

$$\sum_{j=J^B}^{J} \left\{ F_{ij} \cdot \hat{x} \sigma^{inc}(\mathbf{x}_j) \hat{n} - K_{ij}^{11} \cdot u^{inc}(\mathbf{x}_j) - K_{ij}^{12} \cdot v^{inc}(\mathbf{x}_j) \right\}$$

where J^I is the number of node variables inside the heterogeneous region Ω^I. J^B is the node number of the first nodal point lying on the boundary $\partial\Omega^B$. The value of J^B is $J^I + 1$. As before, J is the total number of node points. Finally, J^O is the total number of functions used for the MMP expansion of the outside field. The rows of (47b) follow the same outline. The resulting combined system of equations is of similar form as (21) and can be solved using the same scheme.

$$(51) \quad \begin{pmatrix} \mathbf{K}_{11}^I & \mathbf{K}_{12}^I & \boldsymbol{\Phi}_1^I & \boldsymbol{\Psi}_1^I \\ \mathbf{K}_{21}^I & \mathbf{K}_{22}^I & \boldsymbol{\Phi}_2^I & \boldsymbol{\Psi}_2^I \\ \mathbf{K}_{11}^O & \mathbf{K}_{12}^O & \boldsymbol{\Phi}_1^O & \boldsymbol{\Psi}_1^O \\ \mathbf{K}_{21}^O & \mathbf{K}_{22}^O & \boldsymbol{\Phi}_2^O & \boldsymbol{\Psi}_2^O \end{pmatrix} \cdot \begin{pmatrix} \mathbf{u} \\ \mathbf{v} \\ \phi \\ \psi \end{pmatrix} = \begin{pmatrix} \mathbf{f}_1^I \\ \mathbf{f}_2^I \\ \mathbf{f}_1^O \\ \mathbf{f}_2^O \end{pmatrix}$$

As in the acoustic case, the submatrices K^I resulting from the interior problem are sparse and square. All other submatrices are rectangular. We reduce the above system by Gaussian elimination of the node variables $\mathbf{u}$ and $\mathbf{v}$ which yields a new system.

$$(52) \quad \begin{pmatrix} \tilde{\mathbf{K}}_{11}^I & \tilde{\mathbf{K}}_{12}^I & \tilde{\boldsymbol{\Phi}}_1^I & \tilde{\boldsymbol{\Psi}}_1^I \\ 0 & \tilde{\mathbf{K}}_{22}^I & \tilde{\boldsymbol{\Phi}}_2^I & \tilde{\boldsymbol{\Psi}}_2^I \\ 0 & 0 & \tilde{\boldsymbol{\Phi}}_1^O & \tilde{\boldsymbol{\Psi}}_1^O \\ 0 & 0 & \tilde{\boldsymbol{\Phi}}_2^O & \tilde{\boldsymbol{\Psi}}_2^O \end{pmatrix} \cdot \begin{pmatrix} \mathbf{u} \\ \mathbf{v} \\ \phi \\ \psi \end{pmatrix} = \begin{pmatrix} \tilde{\mathbf{f}}_1^I \\ \tilde{\mathbf{f}}_2^I \\ \tilde{\mathbf{f}}_1^O \\ \tilde{\mathbf{f}}_2^O \end{pmatrix}$$

The lower half of (52) can now be solved in the least squares sense by QR decomposition.

$$(53) \quad \begin{pmatrix} \tilde{\boldsymbol{\Phi}}_1^O & \tilde{\boldsymbol{\Psi}}_1^O \\ \tilde{\boldsymbol{\Phi}}_2^O & \tilde{\boldsymbol{\Psi}}_2^O \end{pmatrix} \cdot \begin{pmatrix} \phi \\ \psi \end{pmatrix} = \begin{pmatrix} \tilde{\mathbf{f}}_1^O \\ \tilde{\mathbf{f}}_2^O \end{pmatrix}$$

The node variables in the heterogeneous, interior region are recovered by back-substitution, the upper half of (52) is already in upper triangular form.

$$(54) \quad \begin{pmatrix} \tilde{\mathbf{K}}_{11}^I & \tilde{\mathbf{K}}_{12}^I \\ 0 & \tilde{\mathbf{K}}_{22}^I \end{pmatrix} \cdot \begin{pmatrix} \mathbf{u} \\ \mathbf{v} \end{pmatrix} = \begin{pmatrix} \tilde{\mathbf{f}}_1^I - \tilde{\boldsymbol{\Phi}}_1^I \phi - \tilde{\boldsymbol{\Psi}}_1^I \psi \\ \tilde{\mathbf{f}}_2^I - \tilde{\boldsymbol{\Phi}}_2^I \phi - \tilde{\boldsymbol{\Psi}}_2^I \psi \end{pmatrix}$$

IMPLEMENTATION

Because the technique is a mixture of MMP expansions and the FE method, the finite element method is merged into the prior MMP codes (Imhof, 1995a,b). Thus, the method is implemented on a nCUBE2 parallel computer using the computer language C++. The object oriented design has the advantage, that the coupling as described in (20) and (50) is basically hidden in objects for node variables, finite elements and the expansion functions for the exterior. First, the objects for the finite elements calculate the local $\tilde{M}$, $\tilde{S}$ and $\tilde{F}$ matrices. Then, the resulting coefficients have mapped into the global equation system. Objects for internal node variables simply map the coefficients $\tilde{K}^{ij}$ for the p_j^I into the global system of equations. In contrast, objects for node variables on the boundary automatically evaluate the MMP expansion at the node point as described in equations (18),(19) or (48),(49), weight the expansion with the appropriate $\tilde{K}^{ij}$ or $\tilde{F}^{ij}$ coefficient and map the resulting coefficients for p_j^O or ϕ_j, ψ_j into the global system.

To reduce numerical noise, the materials are made slightly lossy by adding a small imaginary component ω^I to the angular frequency. If seismograms are calculated by Fourier synthesis, the true amplitude is recovered by a multiplication with $e^{\omega^I t}$.

NUMERICAL RESULTS: ACOUSTICS

As a first test, we simply embed a homogeneous region in a homogeneous fullspace. The wavefield in the embedded region is modelled by FE. The wavefields in the fullspace are expanded into a MMP series. The material parameters in both regions are the same. Hence, all coefficients of the MMP expansion should be zero, while the FE solution should simply interpolate the incoming field. Clearly, due to the discretization of the field in the interior, the solution in the interior will deviate from the incident field and thus, an additional scattered field will be induced. The strength of this induced field is both a function of the number of elements per wavelength and the angle of incidence of the source field. The embedded region consists of $18*18$ elements, each $4m*4m$ in size. The MMP expansion is (2) with $M = 4$ and $N = 4$. Altogether, 36 expansion functions are used. Figure 3 shows the exact position of node points and expansion centers. The source field is a plane wave, where the angle of incidence ranges from $0°$ up to $45°$. As a measure for the error, we use $< (P - P^{inc})/P^{inc}) >$ along the boundary of the inclusion. Starting with 250 elements per wavelength (EPW), the number of EPW is steadily decreased down to 2 EPW. The results are shown in Figure 4. As can be seen, the error increases slowly until the induced fields are of similar size to the source field. Using 10 EPW yields an error of about 5%. Also, the error becomes slightly smaller the more the incident plane wave propagates in the diagonal direction.

To test the accuracy of the MMP-FE technique, we compare the scattering from an acoustic cylinder with the well-known analytical series solution (Pao and Mow, 1973). The velocity inside the cylinder is 3000m/s; the velocity outside the cylinder the velocity

is 2000m/s. In both regions, the density is kept constant at 2000kg/m^3. The radius a of the cylinder is 44m. To simplify the generation of the FE mesh, a square region larger than the actual cylinder is discretized by 24 elements in either direction. Due to the symmetry of the problem, only one multipole (2), where $M = 1$ and $N = 20$, located at the origin, is used. The geometry is shown in Figure 5. The size of the elements is 4m. Two different wavelengths are used: 25m and 100m. Magnitude and phase are presented in Figures 6 and 7. In the case of $ka = 10$, the deviations of the FE-MMP solution from the analytical one are due to the finite element size. Reducing the element size reduces the deviations. Furthermore, the largest deviations correlate with the smallest magnitudes as can be observed in both Figures 6 and 7. This is an effect of the least-squares solving procedure. The solver uniformly minimizes the misfit at each boundary point. Thus, if the average misfit is ϵ, any true field value smaller than ϵ is lost in the misfit. If better accuracy is desired, the solution should be calculated again with the equations scaled by the reciprocal field obtained before. Basically, $\mathbf{A}^{OI}$ and $\mathbf{A}^{OO}$ should be scaled by $\frac{1}{p_i}$. Further details on scaling can be found in the prior paper (Imhof, 1995a).

Lastly, we calculate the seismogram for a complex geometry depicted in Figure 8. The scatterers are roughly 180m long and 35m thick. The velocity and density in the background are 2000m/s and 2000kg/m^3, respectively. The velocity and the density in the two scatterers are 3000m/s and 2000kg/m^3, respectively. Each finite element is 3m by 3m in size. For each scatterer, five centers of expansion are used. At each center $\mathbf{x}_m$, an expansion of the form

$$\sum_{n=-8}^{8} p_{mn}^O e^{in\varphi} H_{|n|}^{(1)} \left(k_O \left| \mathbf{x} - \mathbf{x}_m \right| \right)$$

is set up. The incident field p^{inc} is an explosive line source modulated with a Ricker wavelet (Ricker, 1977) of 50 Hz center frequency. Altogether, 64 receivers will measure the pressure of the scattered field. The resulting seismogram is shown in Figure 9.

NUMERICAL RESULTS: ELASTICS

As in the acoustic case, the first test is to embed a homogeneous region in a homogeneous fullspace. The wavefields in the embedded region are modelled by FE, while the wavefields in the fullspace are expanded into a MMP series. Because the material parameters in both regions are the same, all coefficients of the MMP expansion should be zero and the FE solution should perfectly interpolate the incoming field. Clearly, due to the discretization of the fields in the interior, the solution will deviate from the incident field and thus, additional scattered fields will be induced. The strength of these induced fields is both a function of the number of elements per wavelength and the angle of incidence of the source field. The embedded region consists of $18 * 18$ square elements, each $4m * 4m$ in size. The MMP expansion is the same as (29) with $M = 4$ and $N = 4$.

Altogether, $2 * 36$ expansion functions are used. Figure 3 shows the exact position of node points and expansion centers.

As source fields, we use plane waves of purely P or S polarization. Either experiment is performed twice, first for an angle of incidence of $0°$, then $45°$. Scanning through a range of frequencies allows is to see how polarization, orientation of the elements, and the number of elements per wavelength affect the solution. As a measure for the error, we use $< (|\mathbf{w} - \mathbf{w}^{inc}|)/|\mathbf{w}^{inc}| >$ along the boundary of the inclusion. Again, we start with 250 elements per P-wavelength (EPW) and decrease the number of EPW down to 2. The results are shown in Figure 10. As expected, the errors increase with increasing frequency. Interestingly, incident S waves of very low frequency are less affected than incident P waves of the same frequency. But with increasing frequency, the rate with which the error grows is larger for incident S- than incident P-waves. If less than 5 EPW are used, the S-waves are aliased and the results become meaningless. In general, waves incident at $45°$ are less affected by the grid size than waves incident in the normal direction. Using 25 EPW yields an error of about 8%.

To test the accuracy of the MMP-FE technique in the elastic case, we compare the scattering from a cylinder with the analytical series solution (Pao and Mow, 1973). Inside the cylinder, the P-velocity is 3000m/s and the S-velocity is 1700m/s. Outside the cylinder the P-velocity is 2000m/s and the S-velocity is 1300m/s. In both regions, the density is 2000kg/m^3 and the Poisson's ratio is $\frac{1}{4}$. The radius a of the cylinder is 12m. To simplify the generation of the FE mesh, a square region larger than the actual cylinder is discretized by 24 elements in either direction. Due to the symmetry of the problem, only one multipole (29), where $M = 1$ and $N = 20$, located at the origin, is used. The geometry is shown in Figure 5. The size of the elements is 1m. The wavelength of the incident P-wave is 50m and the wavelength of the incident S-wave is 32m. The magnitude and phase of the u and the v components are shown in Figures 11 and 12. For all incident phases, the match between the analytical solution and the results obtained from the MMP-FE method are excellent.

Lastly, we calculate the seismogram for a complex geometry depicted in Figure 13. A scatterer is illuminated by a line source. The scatterer is roughly 180m long and 35m thick. The P- and S-velocities and density in the background are 2000m/s, 1300m/s and 2000kg/m^3, respectively. The P- and S-velocities and density in the scatterer are 3000m/s, 1730m/s and 2000kg/m^3, respectively. The Poisson's ratio is $\sigma = 0.25$ in both the scatterer and in the background. Each finite element is 2m by 2m in size. In the scatterer, five expansions of the form (29) with $M = 5$ and $N = 7$ are used. Two different incident fields are chosen: a compressional and a rotational line source. Each source is modulated with a Ricker wavelet (Ricker, 1977) of 50 Hz center frequency. Altogether, 64 receivers measure the vertical displacement component of the total field. The resulting seismograms are shown in Figures 14 and 15.

Imhof

SUMMARY

The MMP code has been successfully coupled with the FE method in both acoustic and elastic media. The coupling of the two methods enhances their usefulness for a range of problems. The FE technique allows the simulation of wave propagation in heterogeneous materials. The MMP expansions allow to calculate propagating waves in homogeneous (unbounded) regions in an efficient manner because they commonly need less unknowns to be evaluated and solved for than comparable methods.

Steady-state solutions, as well as seismograms obtained by Fourier synthesis, were calculated for a range of different problems for both acoustic and elastic media. Where available, the solutions obtained by the combined MMP-FEM scheme compared favorably with the analytical solutions.

The combined scheme compensates for the individual weaknesses of MMP and FEM and takes advantage of both their strengths. Thus, the method is well-suited to solve two-dimensional scattering problems for a range of problems which neither method could handle alone.

ACKNOWLEDGMENTS

REFERENCES

Dubus, B., Coupling finite element and boundary element methods on a mixed solid-fluid / fluid-fluid boundary for radiation or scattering problems, *J. Acoust. Soc. Am.*, *96*, 3792–3799, 1994.

Hafner, C., *The generalized Multipole Technique for Computational Electromagnetics*, Artech House, Inc., Boston, 1990.

Hestenes, M.R. and E. Stiefel, Methods of conjugate gradients for solving linear systems, *J. Res. National Bureau of Standards, 49*, 409–436, 1952.

Imhof, M.G., Multiple multipole expansions for acoustic scattering, *J. Acoust. Soc. Am.*, *97*, 754–763, 1995a.

Imhof, M.G., Multiple multipole expansions for elastic scattering, submitted to *J. Acoust. Soc. Am.*, 1995b.

Kelly, K.R., R.W. Ward, S. Treitel, and R.M. Alford, Synthetic seismograms: a finite difference approach, *Geophysics, 41*, 2–27, 1976.

Marfurt, K.J., Accuracy of finite-difference and finite-element modeling of the scalar and elastic wave equations, *Geophysics, 49*, 533–549, 1984.

Murphy, J.E. and S.A. Chin-Bing, A finite-element model for ocean acoustic propagation and scattering, *J. Acoust. Soc. Am., 86*, 1478–1483, 1989.

Murphy, J.E. and S.A. Chin-Bing, A seismo-acoustic finite element model for underwater acoustic propagation, in *Shear Waves in Marine Sediments*, J.M. Hovem, M.D. Richardson, and R.D. Stoll (eds.), Kluwer Academic Publishers, 463–470, Boston, 1991.

Pao, Y.H. and C.C. Mow, *Diffraction of Elastic Waves and Dynamic Stress Concentrations*, The Rand Corporation, New York, 1973.

Ricker, N.H., *Transient Waves in Visco-Elastic Media*, Elsevier Scientific Publishers, Amsterdam, 1977,

Schuster, G.T. and L.C. Smith, A comparison among four direct boundary integral methods, *J. Acoust. Soc. Am. 77* 850–864, 1985.

Schwarz, H.R., *Finite Element Methods*, Academic Press, San Diego, 1988.

Schwarz, H.R., *Numerical Analysis*, Wiley, New York, 1989.

Su, J.H., V.V. Varandan, and V.K. Varandan, Finite element eigenfunction method (feem) for elastic (sh) wave scattering, *J. Acoust. Soc. Am., 73*, 1499–1504, 1983.

Virieux, J., P-SV wave propagation in heterogeneous media: Velocity stress finite difference method, *Geophysics, 51*, 889–901, 1986.

Waterman, P.C., New formulation of acoustic scattering, *J. Acoust. Soc. Am., 45*, 1417–1429, 1969.

Waterman, P.C., Matrix theory of elastic wave scattering, *J. Acoust. Soc. Am., 60*, 567–580, 1976.

Zienkiewicz, O.C., *The Finite Element Method*, McGraw-Hill, New York, 1977.
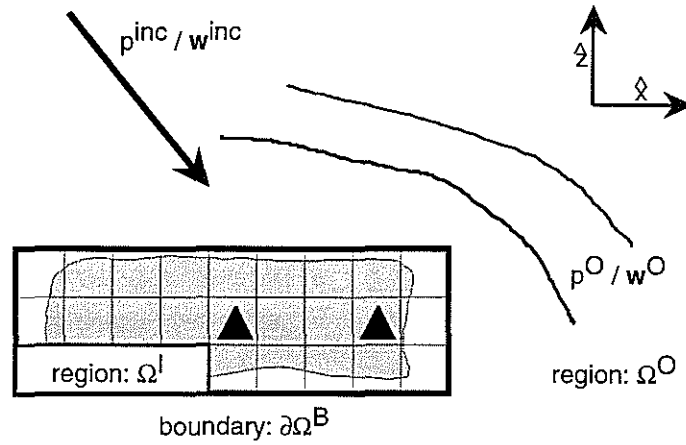
Figure 1: The generic scattering problem to be solved by the hybrid MMP-FEM technique. A heterogeneous scatterer Ω^I is embedded in a homogeneous background Ω^O. In the acoustic case, the incident field is p^{inc} and the scattered field is p^O. In the elastic case, the incident field is w^{inc} and the scattered field w^O. The triangles symbolize expansion centers for the MMP.
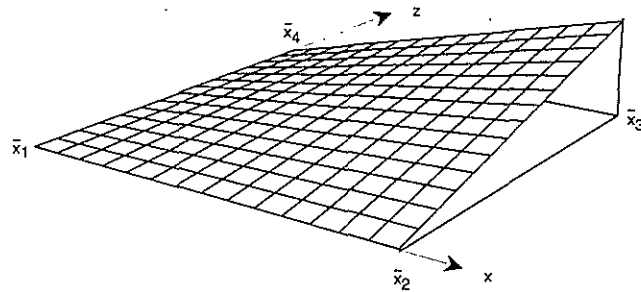

Figure 2: The shape function $\tilde{N}_3(x) = xz$ for a square unit element $\tilde{\Omega}$ and bilinear interpolation. The other shape functions $\tilde{N}_1(x)$, $\tilde{N}_2(x)$ and $\tilde{N}_4(x)$ are obtained by rotations of $-180°$, $-90°$ and $90°$, respectively.
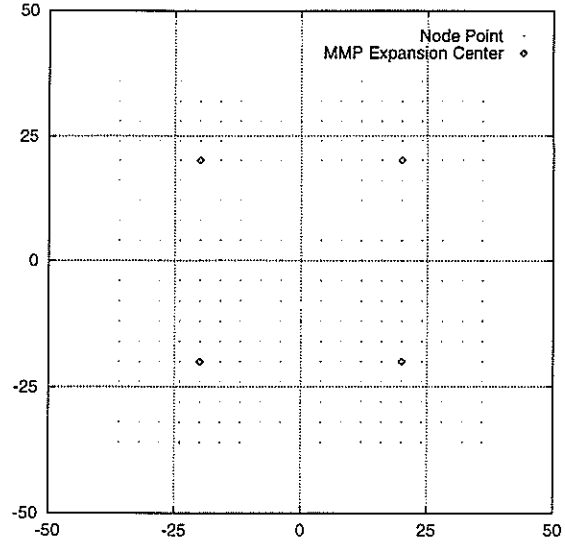
Figure 3: An embedded homogeneous region. Each dot represents a node point and each diamond a MMP expansion center. From each expansion center $\vec{x}_m$, we set up an expansion $\sum_{n=-4}^{4} p_{mn}^{O} e^{in\varphi} H_{|n|}^{(1)} (k_O |\vec{x} - \vec{x}_m|)$.
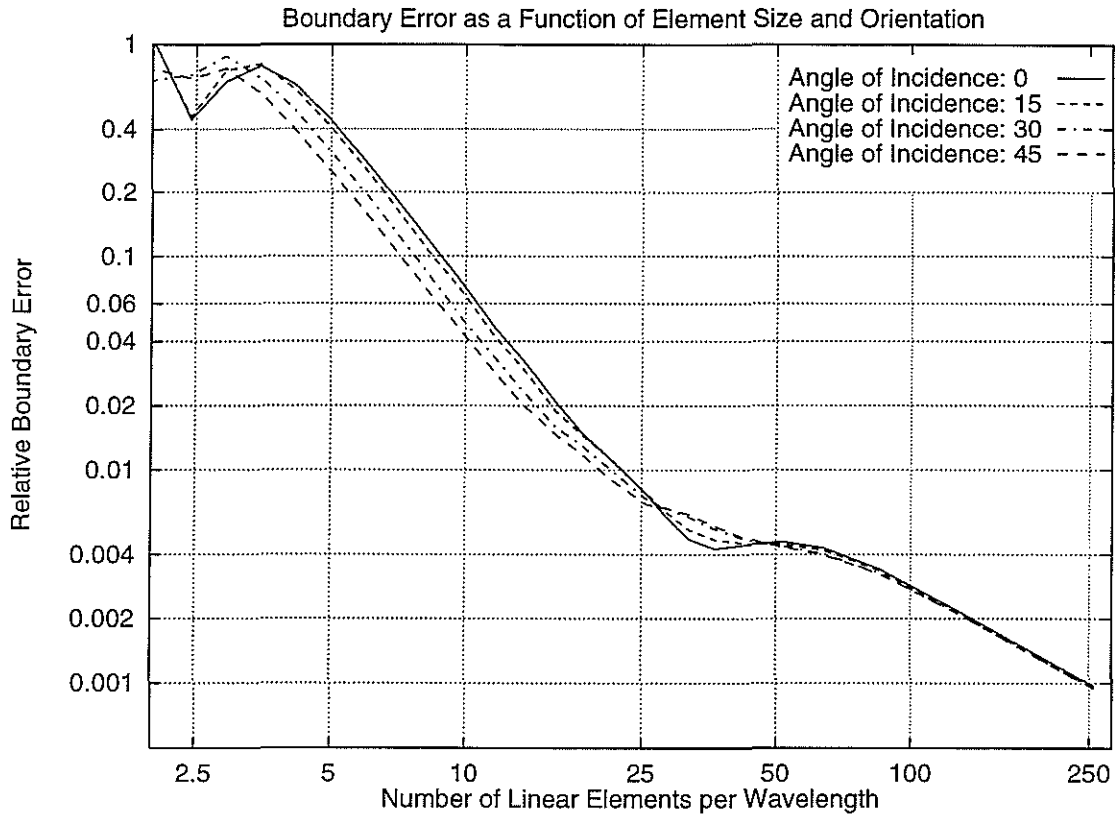
Figure 4: Relative boundary error $< (P - P^{inc})/P^{inc} >$ as a function of the number of elements per wavelength (EPW) and propagation angle of the incident field with respect to the finite elements. 10 EPW yields an error of 5%. Waves propagating diagonally are less affected by larger element sizes.
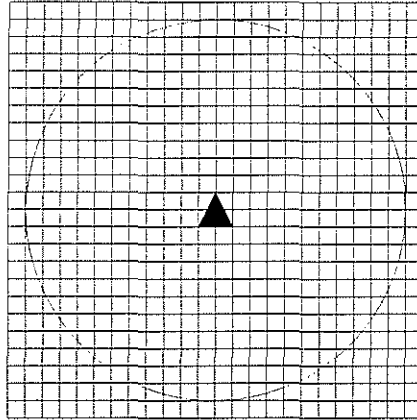
Figure 5: A cylindrical scatterer is illuminated by a plane wave. Outside, the velocity is 2000m/s; inside, the velocity is 3000m/s. The grid represents the finite elements used. The grid spacing is 4m and the radius of the cylinder is 44m. The triangle denotes the expansion center for the multipole.
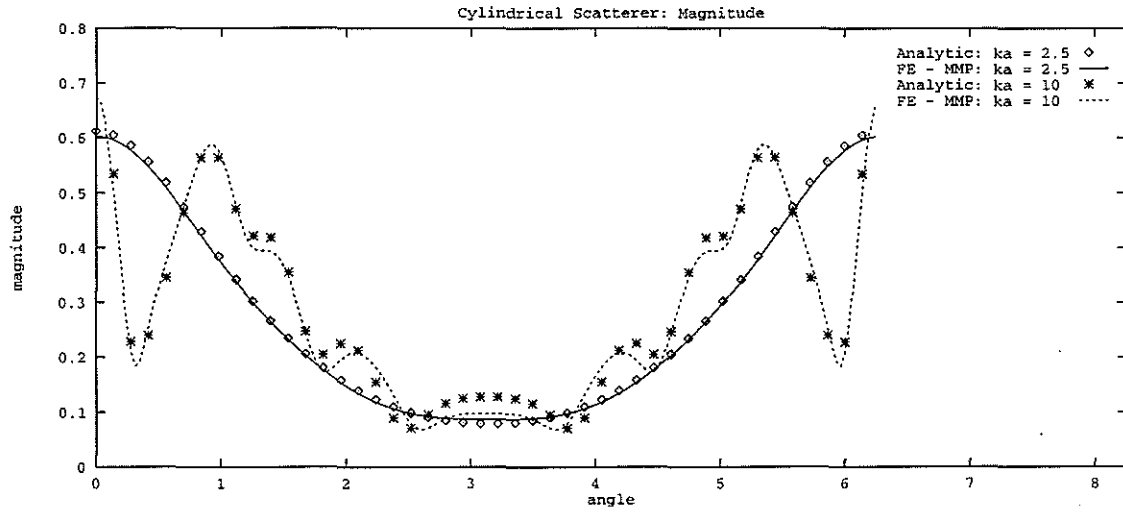
Figure 6: A cylindrical scatterer is illuminated by a plane wave propagating in the positive, horizontal direction. Shown is the magnitude $|P|$ for $ka = 2.5$ and $ka = 10$ as a function of angle.
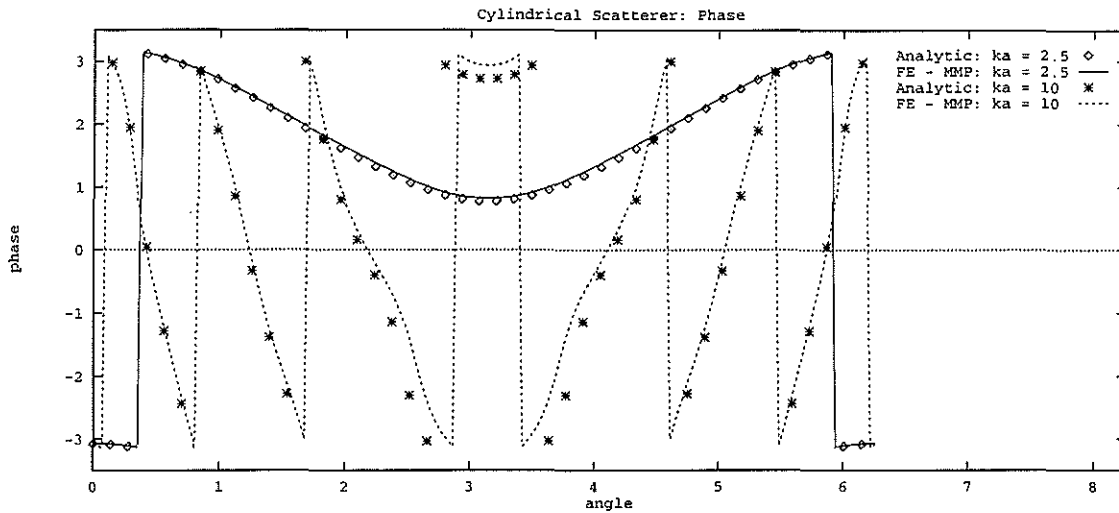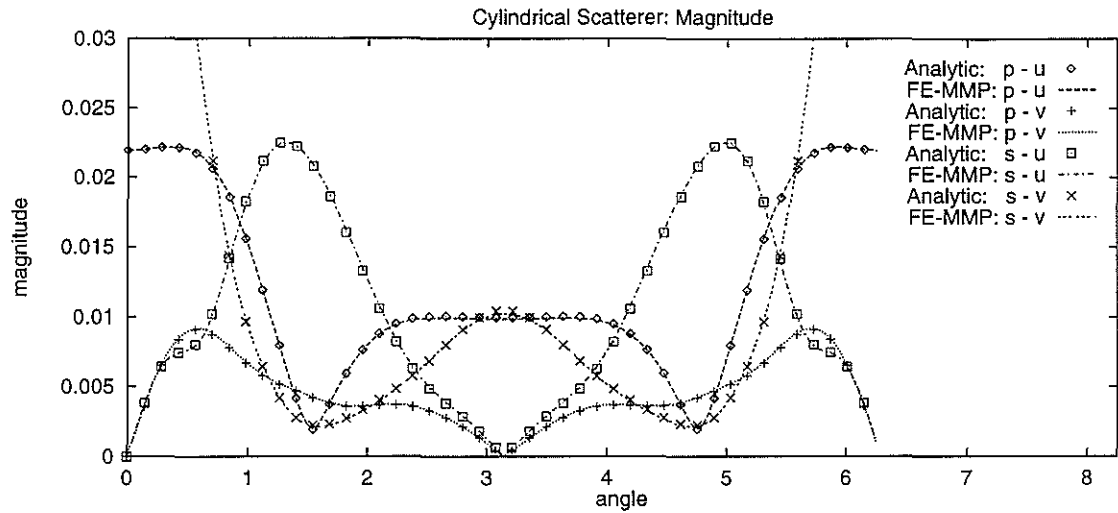
Figure 7: A cylindrical scatterer is illuminated by a plane wave propagating in the positive, horizontal direction. Shown is the phase arg(P) for $ka = 2.5$ and $ka = 10$ as a function of angle.
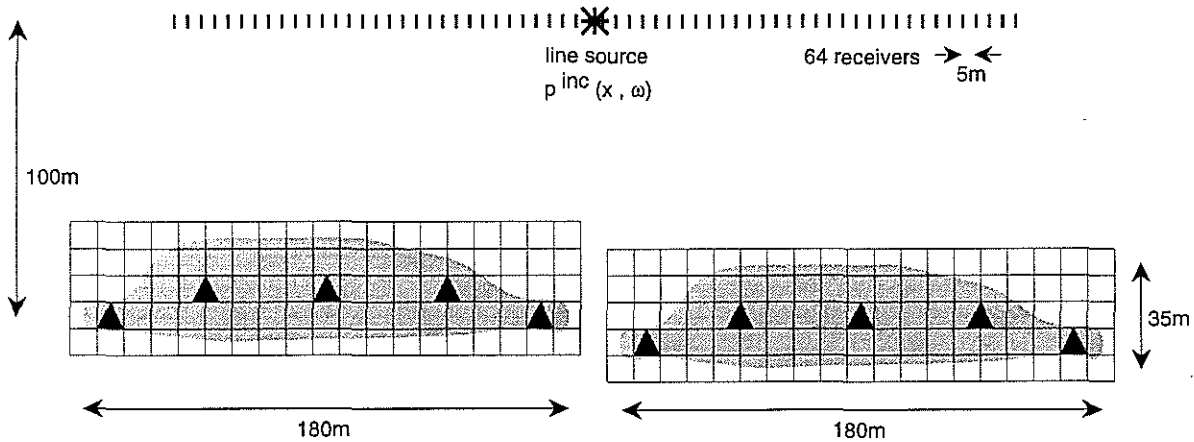
Figure 8: Generic scatterers used to calculate seismograms. Two homogeneous scatterers are embedded in a homogeneous background. The velocity and the density in the background are 2000m/s and 2000kg/m^3, respectively. The velocity and the density in the two scatterers are 3000m/s and 2000kg/m^3, respectively. The triangles show the location of the centers for the MMP expansion.
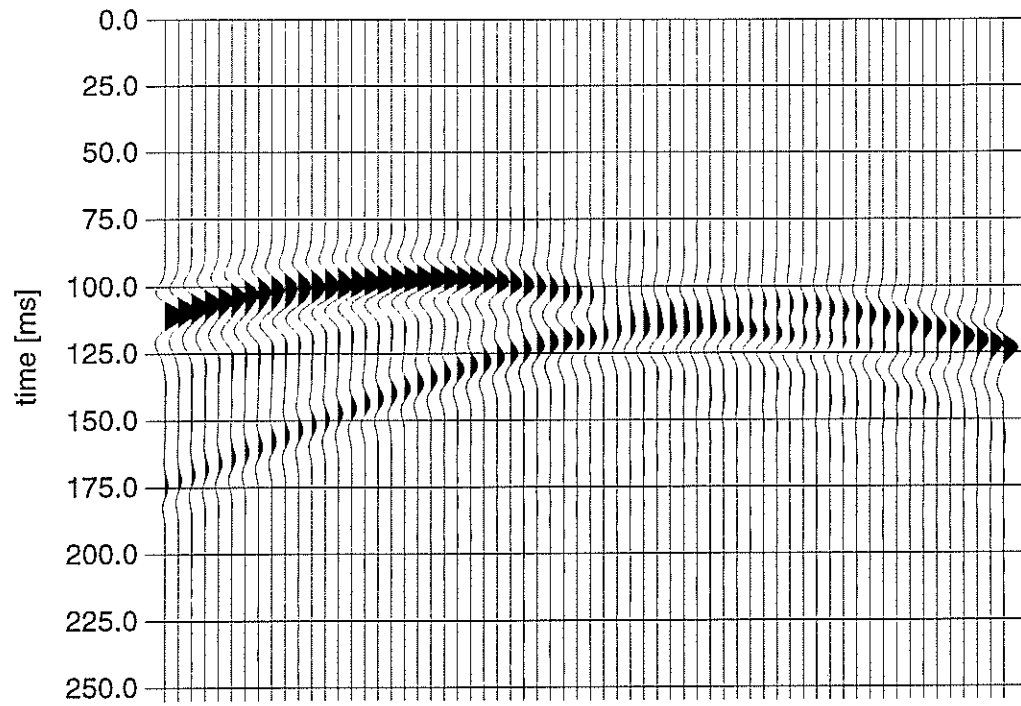
Figure 9: The resulting seismogram for the complex geometry depicted in Figure 8.
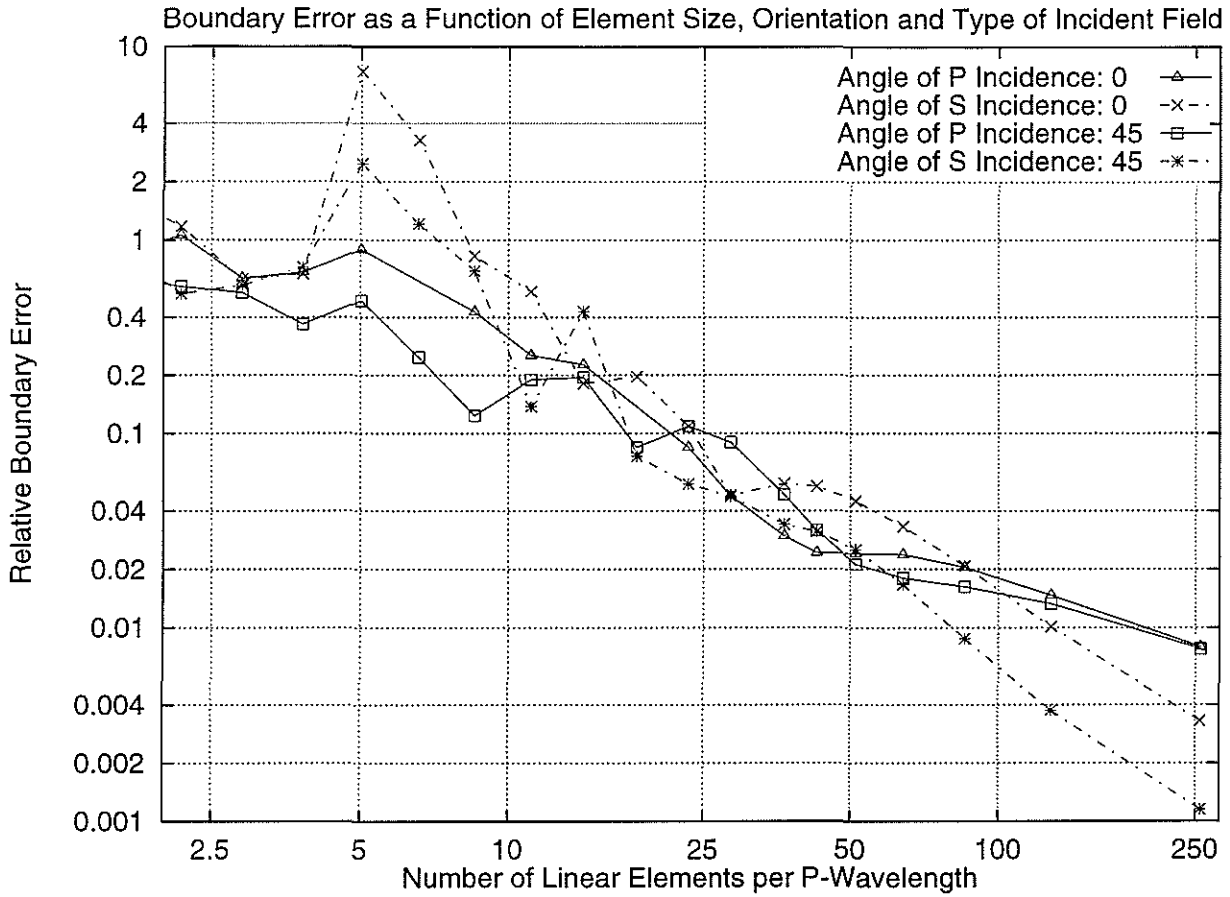
Figure 10: Relative boundary error $< |w - w^{inc}|/|w^{inc}| >$ as a function of the number of elements per P-wavelength (EPW) and propagation angle of the type of incident field with respect to the finite elements. 25 EPW yields an error of 8%. Waves propagating diagonally are less affected by larger element sizes. Also, an incident S wave is more affected by the element size because its wavelength is roughly half as long as the corresponding P wave's.

Cylindrical Scatterer: Magnitude

Figure 11: A cylindrical scatterer is illuminated by a plane wave propagating in the positive, horizontal direction. Both P and S modes are used as incident fields. Shown are the magnitude of $|u|$ and $|v|$ for $ka = 1.5$ and $la = 2.3$ as a function of angle.
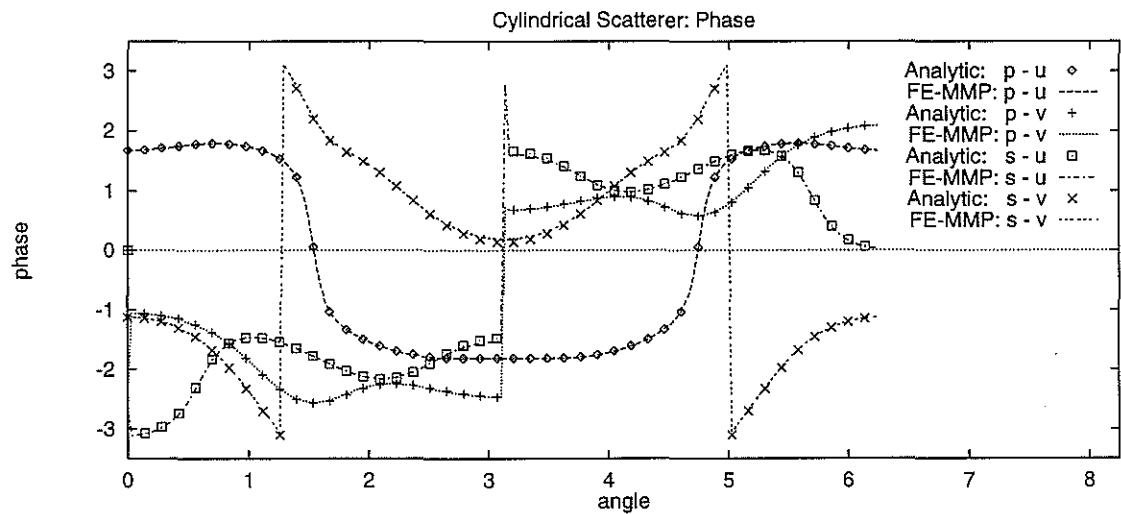
Cylindrical Scatterer: Phase

Figure 12: A cylindrical scatterer is illuminated by a plane wave propagating in the positive, horizontal direction. Both P and S modes are used as incident fields. Shown are the magnitude of $\arg(u)$ and $\arg(v)$ for $ka = 1.5$ and $la = 2.3$ as a function of angle.
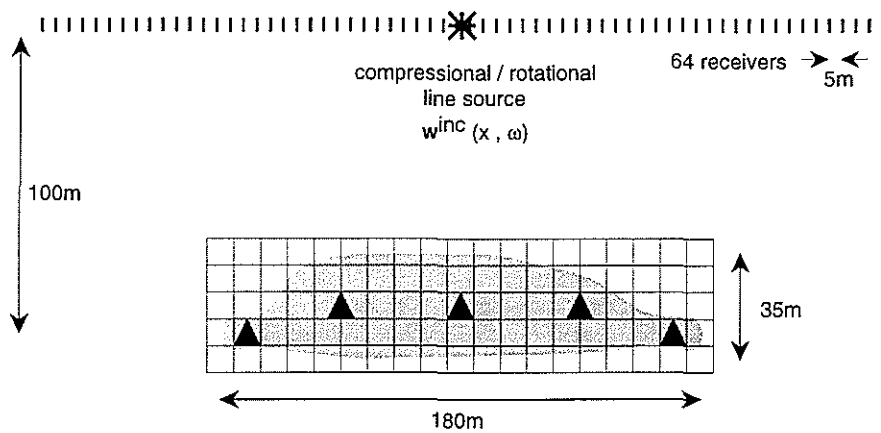
Figure 13: Generic scatterer used to calculate elastic seismograms. The scatterer is embedded in a homogeneous background. The P- and S-velocities and density in the background are 2000m/s, 1300m/s and 2000kg/m³, respectively. The P- and S-velocities and density in the scatterer are 3000m/s, 1730m/s and 2000kg/m³, respectively. Thus, Poison's ratio in the scatter is the same as in the background. The triangles show the location of the centers for the MMP expansion.
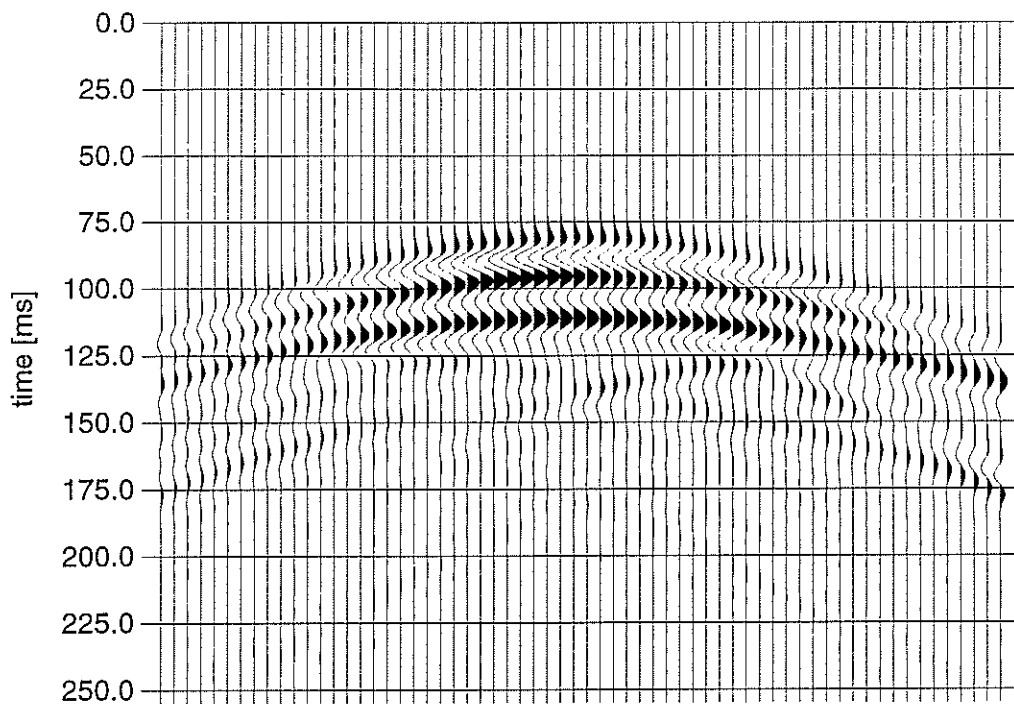
Figure 14: The vertical component of the seismogram for the complex geometry depicted in Figure 13. The incident field is a compressional line source.
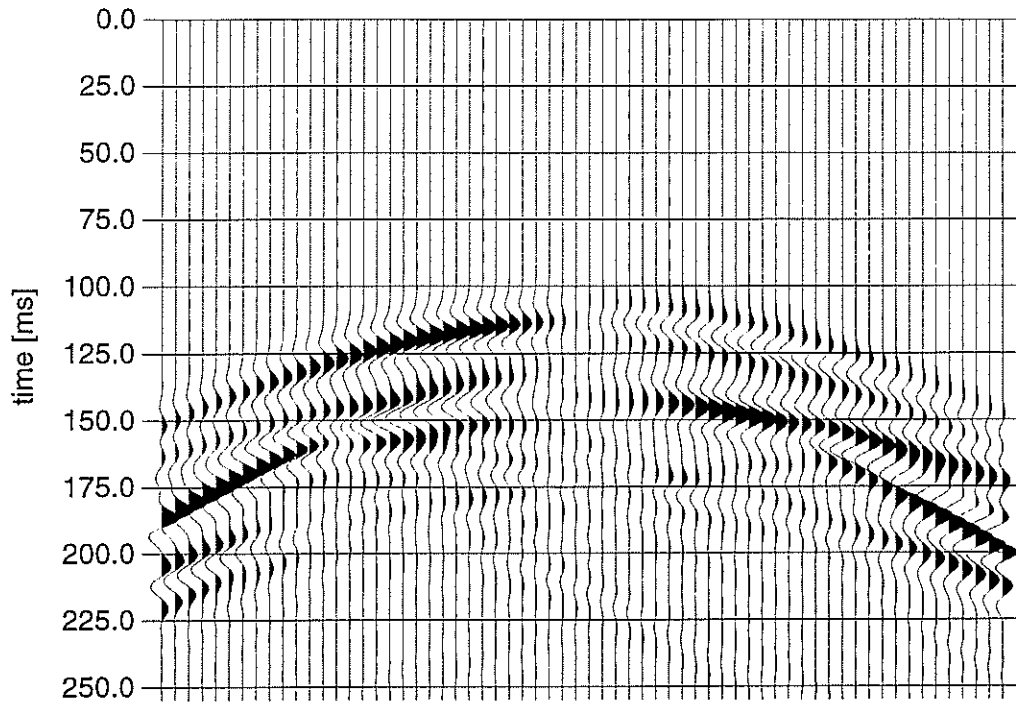
Figure 15: The vertical component of the seismogram for the complex geometry depicted in Figure 13. The incident field is a rotational line source.